

Full length article

Anisotropic deformation characteristics of an ultrafine- and nanolamellar pearlitic steel

M.W. Kapp^{a,*}, A. Hohenwarter^b, S. Wurster^b, B. Yang^a, R. Pippan^a^a Erich Schmid Institute of Materials Science, Austrian Academy of Sciences, Jahnstr. 12, 8700 Leoben, Austria^b Department of Materials Physics, Montanuniversität Leoben, Jahnstr. 12, 8700 Leoben, Austria

ARTICLE INFO

Article history:

Received 13 August 2015

Received in revised form

16 November 2015

Accepted 23 December 2015

Available online xxx

Keywords:

Nanocomposite

High pressure torsion

Strength

Micro compression

Mechanical behavior

ABSTRACT

Micromechanical experiments with $3 \times 3 \times 6 \mu\text{m}^3$ sized micro pillars were used to examine orientation dependencies of the mechanical properties in a severely plastically deformed high strength steel and compared with the undeformed state. For the synthesis, an initially ultrafine-lamellar (UFL) fully pearlitic steel was subjected to high pressure torsion (HPT) transforming the steel into a nanolamellar (NL) composite. Both microstructural states were then tested *in-situ* inside a scanning electron microscope. Within the individual micro pillars, fabricated by focused ion beam milling, the ferrite and cementite lamellae were aligned parallel, normal or inclined to the loading direction. The main findings are: First, the strength and strain hardening capacity is more than doubled comparing the UFL with the NL composite. Second, an anisotropic mechanical response exists in terms of i) strain hardening capacity and ii) stress level at the onset of plateau formation. Third, deformation and localization mechanisms at large compressive strains vary with the lamellae orientation, however they are independent of the lamellae thickness.

© 2016 Acta Materialia Inc. Published by Elsevier Ltd. This is an open access article under the CC BY-NC-ND license (<http://creativecommons.org/licenses/by-nc-nd/4.0/>).

1. Introduction

Nanocrystalline (NC) and ultrafine-grained (UFG) materials have gained a lot of attraction due to their remarkable strength. Different procedures of severe plastic deformation (SPD) have been developed to refine microstructures, such as, equal channel angular pressing (ECAP), accumulative roll bonding (ARB) or high pressure torsion (HPT) [1–4]. Thereby, large amounts of strain can be imposed to the material, which causes a tremendous reduction of the structural sizes. For single phase materials, the grain refinement saturates at several hundred nanometers, whereas, for multiphase materials, even the nanometer regime can be attained, such as for pearlitic steels [5].

Pearlitic steels possess a widespread field of applications, as for instance for rails, cables for suspension bridges or steel cord wires. The great potential to control their strength by tailoring the interlamellar spacing has been extensively discussed [6–8]. Similar to single phase metallic materials, an inverse proportionality between strength and interlamellar spacing was found, also known as modified Hall–Petch effect. Hence, by strongly confining the

dislocation movement in severely deformed pearlitic steels, ultra-high strength materials can be produced [9]. To date, a cold drawn cord wire holds the highest tensile strength of all structural metallic materials with ~ 7 GPa and thereby approaches approximately one third of the theoretical strength limit [10].

A prominent method capable of producing nanostructured materials and so also SPD bulk pearlitic steels is HPT, where a disk-shaped sample is deformed up to large amounts of shear strain [5,11–16]. The microstructural evolution during HPT deformation is characterized by (i) the rearrangement of the colony structure into a well aligned nanolamellar (NL) composite throughout the specimen, (ii) a reduction of the ferrite and cementite lamellae spacing to approximately 25 nm and 2 nm ($\epsilon_{eq} = 8$) [12] and (iii) a disruption of initially unfavorably aligned cementite lamellae. On the atomic scale, a modification of the chemical composition of the cementite phase takes place. Such observations have been initially reported for pearlitic steels after wire drawing [17] and later on also for HPT deformed materials [15,16], suggesting a partial or even full dissolution of the cementite. EELS measurements on the same material as used in this study, support this view by revealing a change in the electron energy-loss near-edge-fine structure of the carbon-rich areas after an equivalent strain of 8 [12].

* Corresponding author.

E-mail address: marlene.kapp@stud.unileoben.ac.at (M.W. Kapp).

As widely known from composite materials, the aligned pearlitic structure is prone to possess orientation dependent mechanical properties. Up to now, the lamellae alignment has been described as an essential deformation characteristic during SPD [8,18,19], however, only few publications deal with the impact of the lamellae alignment and orientation on the mechanical properties, as for instance scrutinized for the fracture toughness [13]. The major challenge in probing the anisotropic mechanical properties of NL pearlitic steels obtained by HPT is to perform technically reliable experiments considering the small sample dimensions delivered by this technique. To our best knowledge, other SPD-processes such as ECAP or ARB cannot provide comparable high strength materials due to technical processing limitations. Another problem arises regarding the comparison with the ultrafine-lamellar (UFL) pearlitic steel of initial interlamellar spacing having a random distribution of the pearlite colonies. A careful selection and mechanical measurement of a distinctive lamellae orientation is experimentally challenging. A micromechanical testing setup, initially developed to investigate sample size effects [20], was found to satisfy both demands and further allows an *in-situ* investigation of the deformation behavior within a scanning electron microscope (SEM).

In this study, *in-situ* micro compression experiments were conducted on a NL pearlitic steel produced by HPT and compared with the undeformed state, which consists of UFL pearlitic colonies. Micro pillars were focused ion beam (FIB) milled with different lamellae orientations with respect to the subsequent loading direction including a normal, parallel and inclined one. The mechanical response, such as strength and strain hardening capacity, as well as the qualitative deformation and failure characteristics were found to be strongly dependent on the lamellae orientation in the NL as well as in the UFL state.

2. Experimental details

A fully pearlitic rail steel R260 with 0.76 wt% C, 0.35 wt% Si, 1 wt% Mn, 0.017 wt% P and 0.014 wt% S was used, consisting of ferrite and cementite lamellae with an average lamellae spacing of 200 nm and a cementite thickness of 25 nm. HPT was used to refine the microstructure and further details concerning the applied HPT deformation procedure can be found in Ref. [21]. The disk-shaped sample had a thickness, t , of 5.9 mm and a diameter of 26 mm, the number of rotations, n , was two and the nominal applied hydrostatic pressure was 5 GPa. The material used for the subsequent micro compression experiments was extracted at a radius r of 12 mm, which results in an equivalent v. Mises strain ε_{eq} of ~ 15 according to Eq. (1)

$$\varepsilon_{eq} = \frac{2\pi nr}{t\sqrt{3}} \quad (1)$$

The ferrite lamellae thickness at $\varepsilon_{eq} = 14.8$ is between 15 nm and 20 nm and the cementite thickness is approximately 2 nm according to earlier TEM work [12,13]. As mentioned earlier, for the described experimental conditions, the chemical composition of the cementite becomes off-stoichiometric during HPT. Nevertheless, for simplicity the term cementite will be maintained for the severely deformed, off-stoichiometric carbon rich phase in the NL pearlitic steel.

Fig. 1 shows the fabrication sequence for the NL micro pillars. For that, a one millimeter thick slice was cut from the HPT disk (Fig. 1a). $3 \times 1.5 \text{ mm}^2$ sized rectangular platelets were cut from this slice in such a way, that the ferrite and cementite lamellae were aligned parallel, normal and inclined (50°) to the later loading direction (Fig. 1b). Subsequently, these platelets were locally thinned

with a Hitachi E-3500 cross section polisher to a wedge of 20 μm thickness [22,23], which facilitates quicker focused ion beam milling (Fig. 1c). Final fabrication of the micro pillars was carried out with a Zeiss LEO 1540 XB dual beam focused ion beam workstation enabling a precise control of the microstructural orientation of the cementite and ferrite lamellae with respect to the pillar axis (Fig. 1d). Therefore, coarse milling currents of 2 nA were used, followed by a final polishing of the pillar surface with 200 pA, in order to reduce the impact of ion damage [24] to the very surface area and to ensure a smooth specimen surface. The taper-free micro pillars are $3 \times 3 \times 6 \mu\text{m}^3$ in size, resulting in an aspect ratio of two, which should prevent plastic buckling [25]. Using the same fabrication process, micro pillars were also cut into single pearlitic colonies of the undeformed UFL material, which were between 10 and 20 μm large, for comparison. Since in this case no macroscopically aligned structure was present (no HPT process was applied), it was required to use a platelet including multiple pearlite colonies with arbitrary orientations and selecting appropriate lamella orientations with the FIB being aligned parallel, normal and inclined (22° and 45°) to the later loading direction.

Micro compression experiments were performed *in-situ* inside a SEM (Zeiss LEO982) in compression mode. An ASMEC UNAT micro indenter with a diamond flat punch indenter tip of 20 μm in diameter was used to load the micro pillars. Misalignment between the micro pillar and the flat punch top surface was minimized by overtilting the pillar top surface by 1.3° during FIB milling.

The micro pillars were loaded under displacement control to total displacements of 1500–3000 nm in either one or two loading steps with a constant initial strain rate of 10^{-3} s^{-1} . Videos were recorded in terms of SEM-image sequences, which were taken every few seconds and allow to link the mechanical data with the material's deformation behavior. Furthermore, post-mortem SEM investigations of each micro pillar side surface were carried out to examine changes in the surface morphology. Cross-sections of the tested micro pillars were obtained by FIB milling and subsequently studied with a SEM in order to gain further insights into the underlying deformation mechanisms of the bulk material.

Supplementary videos related to this article can be found at <http://dx.doi.org/10.1016/j.actamat.2015.12.037>.

The non-specimen related elastic contributions of the measured displacement stemming from the wedge, SEM-stage, specimen holder, as well as from the pillar sink-in Ref. [26] were accounted for by correcting the compliance with a method implemented by Wurster et al. [27]. Finally, engineering stress–strain curves were calculated from the corrected displacement data and the measured force values.

To elucidate the mechanical behavior of the UFL polycrystalline pearlitic steel, compression experiments were performed on comparably large samples with $3 \times 3 \times 6 \text{ mm}^3$. The samples were tested on a conventional testing rig from Zwick with an initial strain rate of $2 \cdot 10^{-4} \text{ s}^{-1}$.

3. Results

3.1. Microhardness measurements

The microhardness distribution within the HPT-processed steel sample increases from the disk center with 270 HV1 by a factor of three to about 740 HV1 at a radius of 12 mm, similarly to [13]. This hardness gradient along the disk radius reflects the gradual decrease of the interlamellar spacing with increasing strain [5]. Under this experimental conditions a hardness plateau, as reported for many pure metals, is not observed, because of an insufficiently high applied deformation strain. Larger number of rotations would lead to a failure of the HPT-anvils or a slipping of the sample within

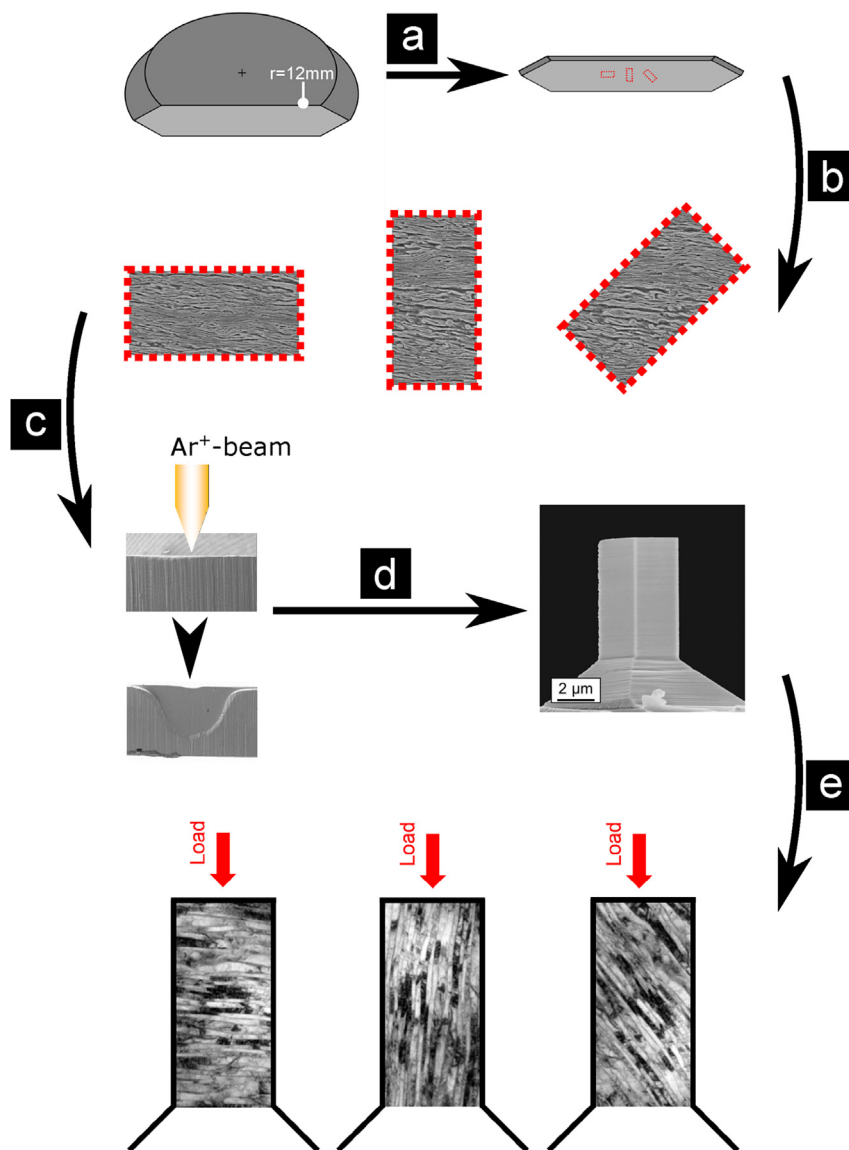


Fig. 1. Fabrication sequence from the HPT disk to the final micro pillars: (a) a 1 mm thick slice is cut from the HPT disk at a radius of 12 mm ($\epsilon_{\text{equ}} \sim 15$). (b) The thin foil is cut into platelets being aligned parallel, normal and inclined with respect to the ferrite and cementite lamellae orientation. (c) These platelets get locally thinned with a cross section polisher. (d) Final shaping of the pillars via FIB milling. (e) In the schematic the final alignment of the pearlitic structure within the micro pillars is depicted (interlamellar spacing is not to scale).

the tool, which would not increase the strain or microstructural fragmentation any further. From the edge area, having a hardness of about 740 HV1, the platelets were extracted.

3.2. Micro pillar testing

The engineering stress–strain curves (first loading step) from the NL and UFL micro pillars, as well as from an UFL macroscopic polycrystalline sample are presented in Fig. 2. Due to experimental artefacts affecting the mechanical data at large strains (i.e. contact between the sheared upper micro pillar half with the sample base increasing the measured force) the main focus lies on the early strain range up to 0.08. This range of interest is presented in Fig. 2 for all tested samples. The full test records are found in the Supplementary.

Stress–strain curves of the UFL micro pillars with the ferrite and cementite lamellae being aligned parallel, normal, inclined under 45° and inclined under 22° to the loading direction are shown in

Fig. 2a up to a strain of 0.08. The accuracy in the determination of the yield point in micro compression experiments is smaller compared to conventional macro-sized experiments, since it is easily altered by misalignment effects of the loading slope (see Supplementary). The yield stress values at a plastic strain of 0.2% are listed in Table 1. For the UFL pillars they are 544 MPa (normal), followed by 604 MPa (45°-inclined), 654 MPa (22°-inclined) and 819 MPa (parallel). The yield stress of the macroscopic polycrystalline sample (549 MPa) is in the same range. The highest yield stress for the parallel orientation should be treated cautiously since a contact problem between the micro pillar and the indenter at the onset of loading (see low slope in insert of Fig. 2a) causes a lower slope in the subsequent elastic regime. However, when macro yielding commences, the impact of this misalignment on the mechanical data diminishes. For comparison the flow stress at 1% and 5% plastic strain as well as the flow stress increase $\Delta\sigma$ from 0.2% to 5% plastic strain and the total applied elongation, ϵ , are listed in Table 1. $\Delta\sigma$ is used as a measure for the strain hardening capacity,

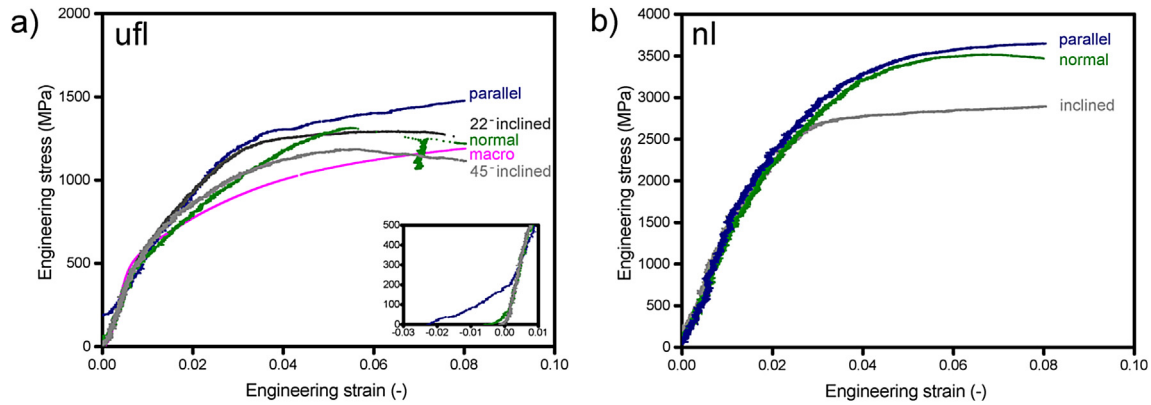


Fig. 2. Engineering stress–strain curves of the a) UFL and b) NL micro pillars with the lamellae orientation parallel, normal, 22°-inclined, 45°-inclined (UFL) and 50°-inclined (NL).

Table 1
The flow stress values $\sigma_{0.2}$, σ_1 and σ_5 at a plastic strain of 0.2%, 1% and 5% as well as the total elongation values ε are listed for the UFL and NL samples. The difference $\Delta\sigma$ of the flow stress values $\sigma_{0.2}$ and σ_5 was calculated as a measure for the strain hardening capacity.

	UFL normal	UFL parallel	UFL 22°-inclined	UFL 45°-inclined	UFL macro-sample	NL normal	NL parallel	NL 50°-inclined
$\sigma_{0.2}$ [MPa]	544	819	654	604	549	1918	1943	1605
σ_1 [MPa]	859	1290	1035	892	734	2890	2848	2375
σ_5 [MPa]	1254	1480	1289	1155	1123	3488	3633	2850
$\Delta\sigma$	710	661	635	551	574	1570	1690	1245
ε [%]	26.6	17.0	20.2	31.3	21.0	27.6	38.5	32.7

considering that pronounced strain localization is not observed before 5% plastic strain. Strain hardening ranges from 551 MPa (45°-inclined), over 635 MPa (22°-inclined) and 661 MPa (parallel) to 710 MPa (normal). In the plateau region, the different orientations require different flow stress levels. The parallel micro pillar deforms at the highest flow stress, showing slight hardening, followed by the 22°-inclined, the normal and the 45°-inclined one, showing slight softening. In short, for the UFL pearlitic steel the lamellae orientation has a substantial influence on the stress–strain response in terms of the strain hardening behavior and the flow stress in the plateau regime.

An anisotropy of the strain hardening capacity and the plateau stress is observed for the NL pearlitic steel in Fig. 2b as well. Contrary to the UFL case, the parallel and normal lamellae orientation show a similar hardening capacity and also the onset of yielding is about the same. For the inclined NL micro pillar the yield stress is about 300 MPa lower and also the strain hardening capacity $\Delta\sigma$ is 325 MPa–445 MPa smaller compared to the normal and parallel ones, respectively. The only difference between the parallel and normal orientation becomes visible in the evolution of the flow stress in the plateau regime, where slight softening is observed for the normal orientation, but the parallel one shows slight hardening.

Comparing the UFL and NL pearlitic steel of the corresponding lamellae orientation a doubling (inclined, parallel) or even triplication (normal) of the yield stress at 0.2% plastic strain is observed in the NL pearlitic steel. Also the strain hardening capacity in terms of $\Delta\sigma$ is increased for the NL pearlitic steel, which is for the NL parallel orientation even 2.5 times higher than for its UFL counterpart.

3.3. SEM characterization of the deformed microstructure after testing

In Fig. 3, the surface morphologies of the UFL and NL micro pillars at different plastic strains ε_{pl} are presented (see Supplementary for additional video sequences). Irrespective of the

interlamellar spacing and lamellae orientation the strain is not homogeneously distributed along the micro pillar height at total nominal strains larger than 0.15 but rather concentrated in more or less narrow bands. For the UFL pearlitic steel this strain localization occurs as multiple small kink bands (parallel, see Fig. 3a) or shear bands (normal and inclined, see Fig. 3b and c). A similar behavior is observed for the NL pearlitic steel. For the parallel orientation (see Fig. 3d) plastic strain localizes in a single, but more extended kink band and for the normal and inclined orientation in narrow shear bands, Fig. 3e and f.

The different nomenclature for kink and shear band becomes plausible by incorporating the SEM images taken from the pillar cross sections for the UFL (Fig. 4a–c) and NL pearlitic steel (Fig. 5a–c) into the discussion. Although the surface morphologies for the UFL parallel and normal orientation appear to be similar, their bulk appearance and thus the underlying deformation characteristics are different. In the case of the parallel orientation, localized bands appear inclined to the pillar axis (see left side surface in Fig. 3a) and exit as straight lines on the neighboring side surface (see right side surface in Fig. 3a). From the cross section in Fig. 4a, it can be inferred that the shear to the left requires local buckling events of the harder cementite phase (marked by arrows), which takes place in the area of the localized bands. Since the cementite lamellae buckle or kink in a cumulative manner (see schematic in Fig. 4a) along the whole pillar width these bands are denoted kink bands. Although SEM images of the surface (Fig. 3a–c) suggest similar localization also for the normal and inclined orientations, the SEM images of the cross sections reveal different deformation mechanisms of the cementite (Fig. 4b and c). The magnified view in Fig. 4b shows the major shear band for the normal orientation, where bending and massive elongation of the cementite lamellae in the shearing direction is visible, making it plausible to denote this structure as shear band. The interlamellar spacing within the shear band of the UFL pillar has been significantly reduced compared to the sample volume above and below the shear band. Due to the larger imposed strain to the inclined

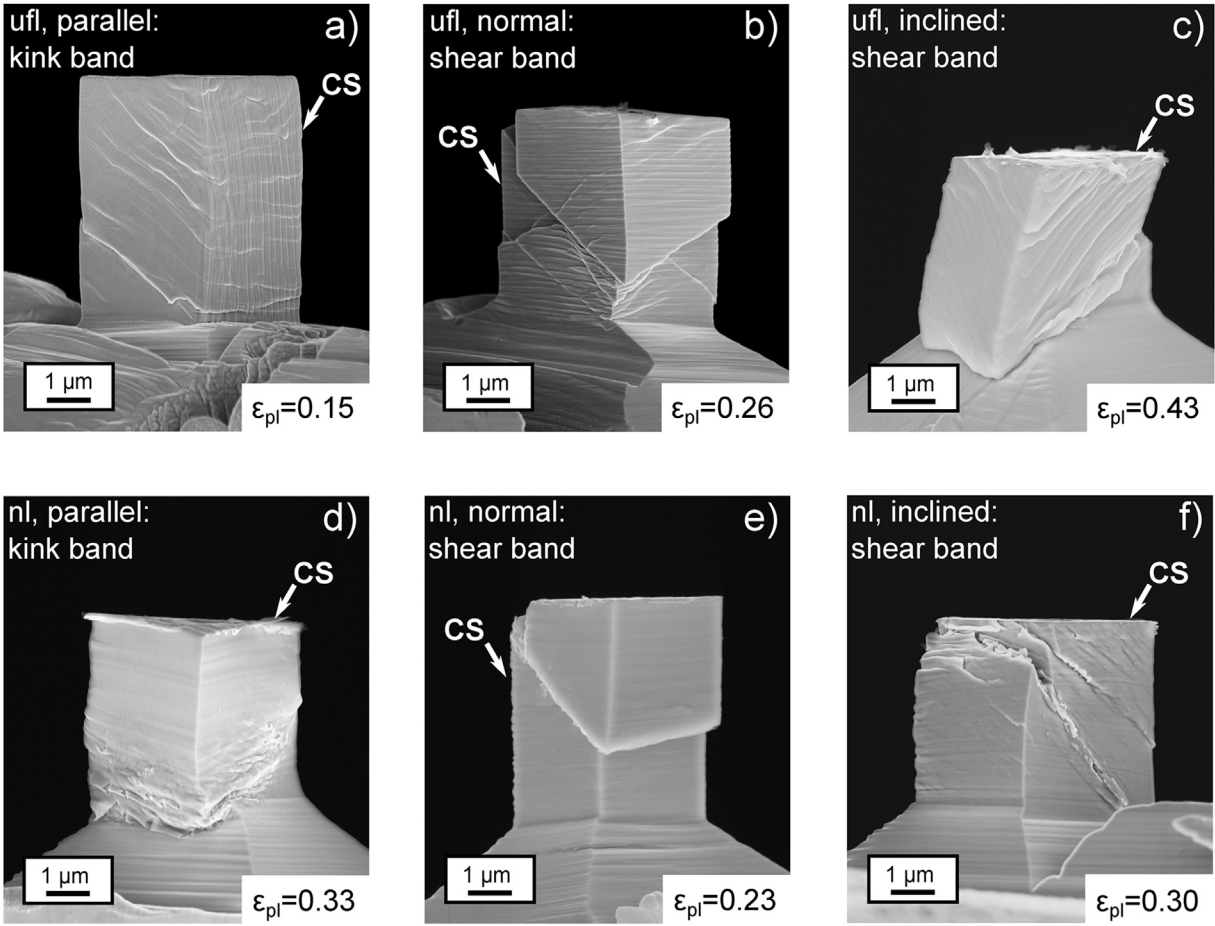


Fig. 3. SEM images of the UFL a–c) and NL d–f) micro pillars after the final deformation step with the lamellae being aligned a,d) parallel, b,e) normal, c) 45°-inclined and f) 50°-inclined with respect to the loading axis. Note that the SEM images of the individual micro pillars were taken at different plastic strains (see inserts). Side surfaces further investigated by FIB milled cross sections presented in Figs. 4 and 5 are marked with CS.

orientation, the deformation characteristics visible in the cross section in Fig. 4c demand careful interpretation: i) lamellae in region 1 are parallel to the initial lamellae orientation and are still preserved as in the pillar base region 2, ii) lamellae in region 3 start

to heavily bend at large strains above 20%, supposedly supported by friction between pillar top and flat punch, iii) in region 4 fragmentation of the cementite lamellae occurs within the major shear band, iv) cementite lamellae remain consistent at the pillar top

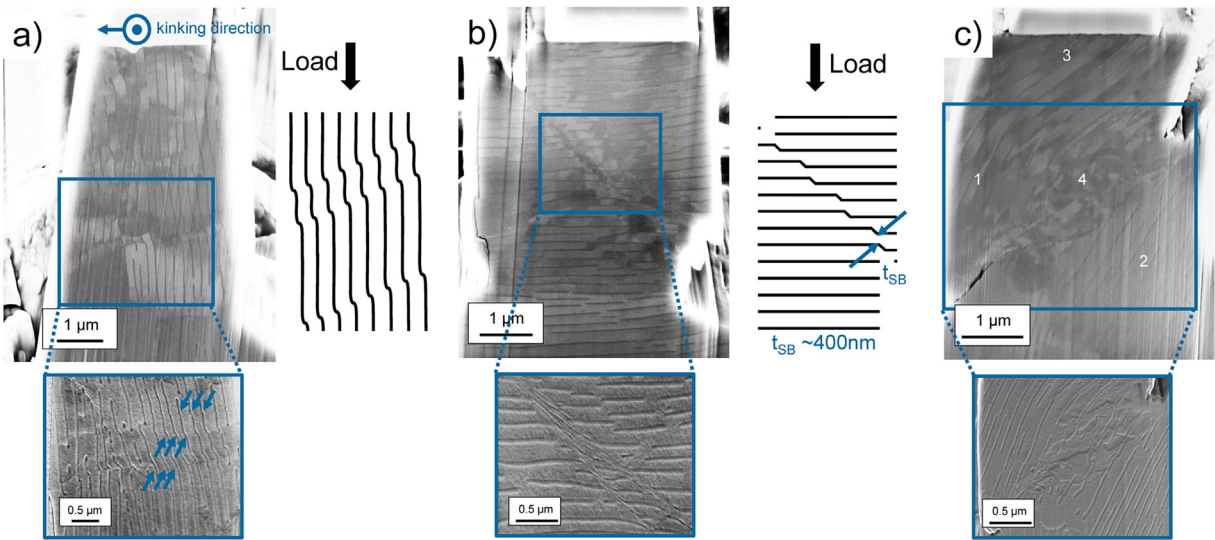


Fig. 4. Cross-sectional investigations were performed parallel to the side surfaces of the a) parallel, b) normal and c) 50°-inclined oriented UFL micro pillars (same as in Fig. 3a–c). Subsequent SEM investigations on these cross sections reveal different deformation characteristics for the individual lamellae orientations. A schematic picture is depicted for two of the different deformation processes.

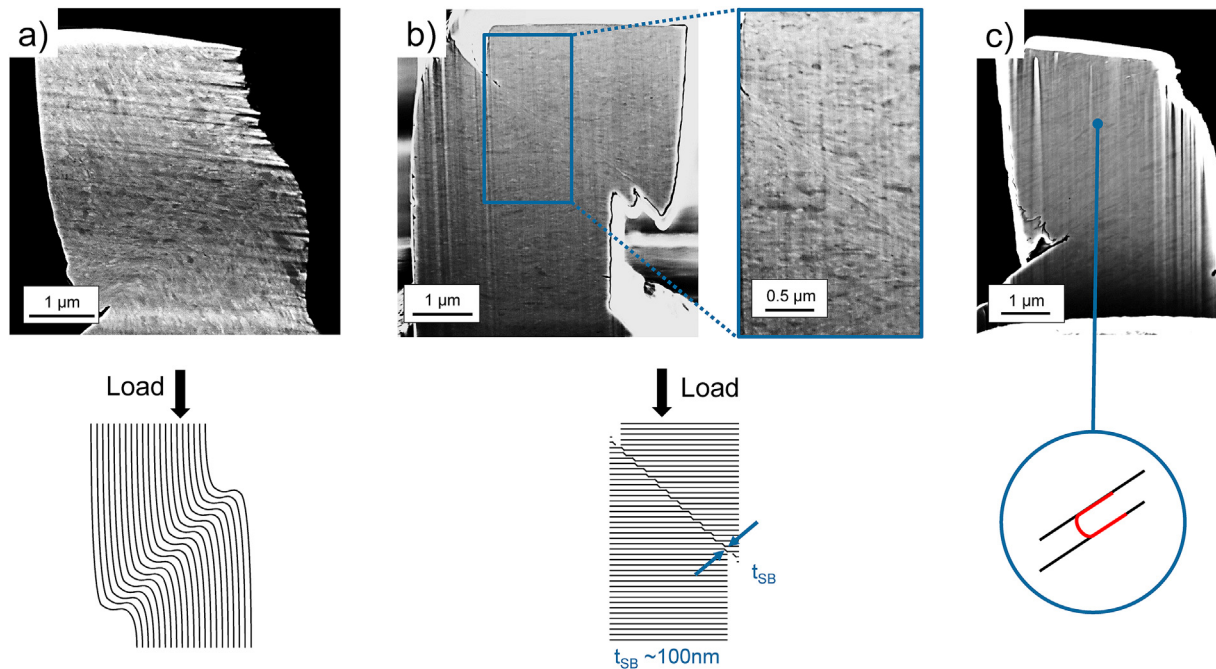


Fig. 5. Cross-sectional investigations were performed parallel to the side surfaces of the a) parallel, b) normal and c) 45°-inclined oriented NL micro pillars (same as in Fig. 3d–f). Subsequent SEM investigations on these cross sections reveal different deformation characteristics for the individual lamellae orientations. A schematic picture is depicted for the three different deformation processes: a) kink formation, b) shear banding, c) dislocation segment moving parallel to the lamellae (confined layer slip).

(region 1, 3), where smaller shear bands realize a smaller amount of strain compared to the major one.

A description of the cross section SEM images of the NL pillars, see Fig. 5, are complicated due to their small interlamellar spacing and the limited resolution provided by the SEM. Despite these difficulties, a description of the deformation characteristics from the SEM images is attempted, as they provide a valuable input in understanding deformation instabilities for NL pearlitic structures. The deformation of the parallel oriented micro pillar is characterized by a kinking of the nanoscaled lamellae in Fig. 5a similar to its UFL counterpart, although here multiple small kink bands are displaced by a single large one, see also schematic in Fig. 5a. This large kink band also controls the shape of the micro pillar presented in the corresponding surface SEM image (Fig. 3d). Whereas the lamellae at the pillar top are almost parallel, they are perpendicularly aligned in the middle part, before they continue their parallel progression towards the pillar base. The strain imposed to the normal oriented pillar is sustained by shearing the upper against the lower pillar half in a very localized shear band (see Fig. 5b). The magnified cross section SEM image of the shear band reveals a bending of the ferrite lamellae in the shearing direction within a thickness of roughly 100 nm, whereas the upper and lower pillar half seem to be unaffected by this localization process. It cannot be determined whether the cementite is bent or broken. Within the shear bands of the inclined pillar orientation in Fig. 5c the lamellae do not show signs of bending, nor kinking, but rather retain their orientation. It is important to point out that localized deformation processes for the UFL and NL micro pillars, obvious in the presented SEM images, did not occur before 5% total strain, which could be inferred from the video sequences.

4. Discussion

The mechanical response presented in the stress–strain curves varies according to the interlamellar spacing (UFL and NL) and the lamellae orientation with respect to the loading direction (parallel, normal, inclined). The main differences can be found in i) the

increased yield stress of the NL compared to the UFL micro pillars, ii) the large differences in the hardening capacity of the different lamellae orientations, as well as their iii) different flow stress levels for the onset of localized deformation, iv) the flow stress evolution in the plateau regime, and v) the orientation dependent deformation mechanism during localization. These peculiarities will be in the center of the following discussion:

4.1. Onset of yielding

Surprisingly, within one microstructural state the yield stress, $\sigma_{0.2}$, is not significantly affected by the lamellae orientation and ranges between 550 and 650 MPa for the UFL state and 1600–1900 MPa for the NL state. However, there are large differences between the UFL and NL microstructures, where an increase of 1374 MPa (normal), 1124 MPa (as a lower bound for parallel) and 1001 MPa (50°-/45°-inclined) occurs depending on the corresponding lamellae orientations. In literature, the origin of the pronounced strength increase of nanolaminates caused by severe plastic deformation is controversially discussed [10,28,29]. The main mechanisms considered for SPD pearlitic steels are dislocation confinement following a Hall–Petch relation or Orowan bowing of single dislocations, solid solution hardening and Taylor hardening. These mechanisms are discussed regarding the main structural changes during high pressure torsion or wire drawing, which are the decrease of the ferrite and cementite lamellae spacing [12], a potential increase of the dislocation density similar to pearlitic wires [29] and the dissolution of the cementite [12]. The dominating mechanisms controlling the increase in strength will be discussed in more detail in the following.

The explanations usually used for the strengthening effect of a refined grain size or lamellar structure are the Hall–Petch and Orowan concepts. A simple estimation of their applicability can be done by setting the ferrite lamellae spacing (exemplarily for normal orientation) in the UFL, d_f^{ufl} , and NL state, d_f^{nl} with the corresponding yield stresses σ_y^{ufl} and σ_y^{nl} into relation. Both values for $\sigma_{0.2}$ ($\sigma_y^{nl,ufl} = \sigma_{0.2}^{nl,ufl} - \sigma_{friction}$) need to be reduced by the friction stress

$\sigma_{friction}$, which is around 120 MPa for pure iron [30]. The ratio NL to UFL yields to:

$$\frac{\sigma_y^{nl}}{\sigma_y^{ufl}} \sim \frac{1798}{424} \sim 4.2 \quad (2)$$

In the UFL-state, d_f^{ufl} is approximately 200 nm and in the NL state, d_f^{nl} is in the range between 15 and 20 nm. For classical dislocation pile-up behavior (Hall–Petch) one can write:

$$\frac{\sigma_y^{nl}}{\sigma_y^{ufl}} \sim \frac{\sqrt{d_f^{ufl}}}{\sqrt{d_f^{nl}}} = \frac{\sqrt{200}}{\sqrt{15}} \div \frac{\sqrt{200}}{\sqrt{20}} \sim 3.7 \div 3.2 \quad (3)$$

For confined layer slip (Orowan):

$$\frac{\sigma_y^{nl}}{\sigma_y^{ufl}} \sim \frac{d_f^{ufl}}{d_f^{nl}} = \frac{200}{15} \div \frac{200}{20} \sim 13.3 \div 10.0 \quad (4)$$

From the simple estimation it seems that the Hall–Petch concept approaches better to the observed behavior. However, we believe that the classical Hall–Petch explanation cannot be used to explain the yield strength of the NL structure, because the lamellar spacing is too small to allow for a pile-up formation. This is supported by results from the multilayer community [31], where it is well known that at a critical lamellae spacing, a transition from the classical pile-up formation following Hall–Petch law to confined layer slip following the Orowan mechanism occurs.

A similar estimate can be done in order to assess the impact of the dislocation density. Taking a dislocation density ρ_f^{nl} of $8.8 \cdot 10^{15} \text{ m}^{-2}$ for the NL and ρ_f^{ufl} of $7.5 \cdot 10^{13} \text{ m}^{-2}$ as a higher bound for the UFL state from Zhang et al. [29] we obtain:

$$\frac{\sigma_y^{nl}}{\sigma_y^{ufl}} \sim \frac{\sqrt{\rho_f^{nl}}}{\sqrt{\rho_f^{ufl}}} = \frac{\sqrt{8.8 \cdot 10^{15} \text{ m}^{-2}}}{\sqrt{7.5 \cdot 10^{13} \text{ m}^{-2}}} \sim 10 \quad (5)$$

The pre-factor, α , and the shear modulus, G , in the Taylor relation $\Delta\sigma = \alpha G b \sqrt{\rho}$ might be different for the undeformed and the HPT deformed state, but the required large difference would be difficult to explain on a solid physical basis. Similar to the Orowan estimate, the Taylor hardening approach clearly overestimates the observed yield strength increase from the UFL to the NL state and justifies that it cannot be the solely strength controlling factor.

A further hardening mechanism could be related to the dissolution of the cementite, reflected by a small increase of the carbon concentration within the ferritic phase [10,16], which was inferred from EELS measurements in the present pearlitic steel [12]. Recently, Li et al. [10] showed that the main effect of the carbon segregation on strength is the stabilization of the ferritic subgrain structure. Hence, the nanosized subgrain structure is stabilized up to large strains and thereby confine dislocation glide paths, which further results in a tensile strength of up to 7 GPa. However, these findings become only relevant at smaller structural sizes as in the current case and should not play the dominant role in this work, where the lamellar structure with a larger interlamellar spacing between 15 and 20 nm is still present.

The foregoing estimates and comparison of the results indicate that a single strength and hardening controlling mechanism cannot fully explain the difference between the NL and UFL pearlitic steel. Nevertheless, it is evident that in the NL state the ferrite lamellae spacing is the main microstructural feature governing the yield strength.

4.2. Strain hardening

NL and UFL pearlitic steels exhibit a strong hardening [32] up to a certain plastic strain between 1.7% and 3.4%, depending on the lamellar orientation and lamellae spacing. However, there are significant differences in the orientation dependence and the amount of hardening in the NL and UFL structure.

4.2.1. UFL pearlitic steel

The stress–strain curves in Fig. 2a and idealized in Fig. 6a consist of three different regimes. Therefore, we assume the occurrence of three deformation modes (see Fig. 6a, numbered dots) similarly as reported by Thilly et al. for Cu–Nb wires [33]: 1) Elastic behavior below the ferrite yield point (F, see Fig. 6a); 2) Plastic and elastic behavior of the ferrite and cementite, respectively, above the ferrite yield point (F); 3) Plastic behavior of both phases beyond the cementite yield point (C, see Fig. 6a). The major amount of hardening is realized for all lamellae orientations in deformation mode 2.

Loading parallel to the lamellae exhibits a significant stronger hardening rate compared to the normal and inclined orientation. In both cases the hardening is nearly linear between the yield points of the ferrite (F) and cementite (C). This indicates that a very simple composite model with plastic ferrite lamellae and linear elastic cementite lamellae can be used to explain the hardening and orientation dependence. Thus, for the parallel loading, the flow stress $\sigma_f(\varepsilon)$ can be calculated according to

$$\sigma_f(\varepsilon) = \sigma_f^f(\varepsilon) * f^f + E^c * \varepsilon * f^c \quad (6)$$

where $\sigma_f^f(\varepsilon)$ is the strain dependent flow stress of the ferrite, f^f the ferrite fraction, E^c the Youngs modulus of the cementite, ε the applied strain and f^c the fraction of the cementite. The limit of this strong hardening is determined by the plastic deformation or the plastic buckling of the cementite lamellae, as shown in Fig. 4a, when the applied strain equals the yield strain of the cementite ($\varepsilon = \varepsilon_y^c$), which is $\varepsilon_y^c \sim 1.5\%$ at $\sigma_y^c \sim 3 \text{ GPa}$ [34]. In other words, the high yield stress of the cementite σ_y^c stabilizes dislocation multiplication within the ferritic phase as schematically shown in Fig. 7a, which requires the co-deformation of both phases. Once a kink band forms at the end of deformation mode 2 (see video sequences in the Supplementary), pronounced strain hardening terminates.

For the loading perpendicular to the lamellae, the plastic deformation of the ferrite in deformation mode 2 (see Fig. 7b) is constrained by the lateral flow which is confined by the elastic lateral deformation of the cementite. Assuming the Youngs' moduli of the ferrite and cementite are about the same $E^f \sim E^c$, furthermore, the yield stress of the ferrite σ_y^f is very small compared to the cementite σ_y^c and the volume fraction of the cementite f^c is small compared to the ferrite f^f , a very simple relation can be used to estimate the early hardening until yielding of the cementite starts at the onset of the stress plateau:

$$\sigma_f(\varepsilon) = \sigma_f^f(\varepsilon) * f^f + \frac{1}{2} * E^c * \varepsilon * f^c \quad (7)$$

The second term describes the increase of flow stress due to the constrain in lateral flow of the ferrite (the hydrostatic stress component). The plastic strain in lateral direction, $\varepsilon_{lateral}$, is half of the one in the loading direction, ε , since in the fully plastic range the lateral contraction of the ferrite can be set to 0.5 ($\varepsilon_{lateral}/\varepsilon = 0.5$). The limit of this strong hardening is reached when the cementite starts to deform plastically at $\varepsilon = 2\varepsilon_y^c$.

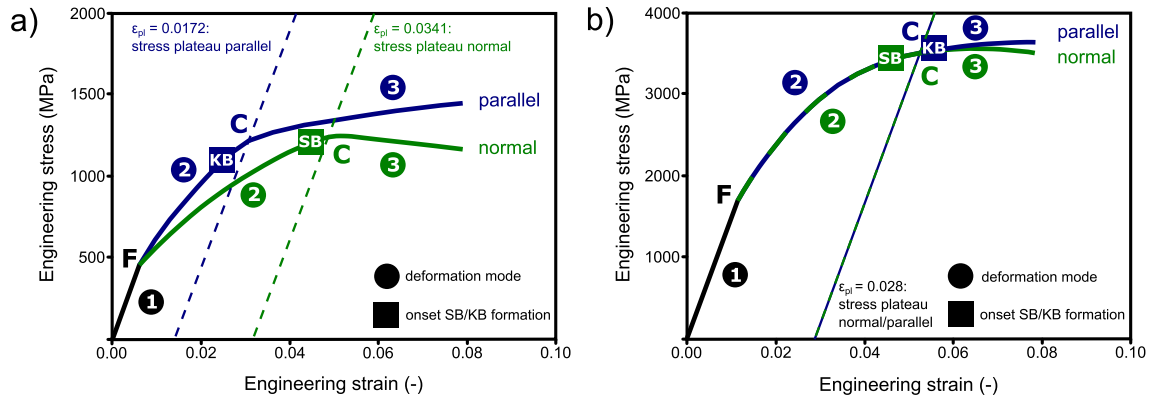


Fig. 6. Schematic of stress–strain curves of the parallel and normal oriented a) UFL and b) NL micro pillars, where squares mark the formation of the dominant shear band (SB) or kink band (KB). The dotted lines mark the plastic strain where plateau formation for the parallel and normal orientation is observed.

4.2.2. NL pearlitic steel

Similar to the UFL state the major amount of strain hardening is realized in the regime, where the ferrite lamellae deform plastically and the cementite stays elastic (see Fig. 2b and idealized Fig. 6b). However, the early hardening in the NL pearlitic steel is significantly larger than in the UFL microstructure. This indicates that the reduced lamellae thickness does not allow for a simple dislocation pile-up model anymore, but favors plasticity carried by single dislocations, moving from one boundary to another [35,36]. This is also supported by reconsidering Section 4.1 which showed that the strength in the NL state does not fully correspond to the dislocation pile-up approach. To realize a plastic strain of 2.8% (see Fig. 6b) in the 15 nm or 20 nm thick ferrite lamellae, one or two dislocations need to be pushed through the lamellae until the leading segment is stored in the opposite interface as schematically shown in Fig 7c. Multiple activation of dislocations along the ferrite lamellae could account for the in the experiment observed homogenous deformation up to a flow stress of more than 3 GPa tremendous hardening (see Supplementary for video sequences).

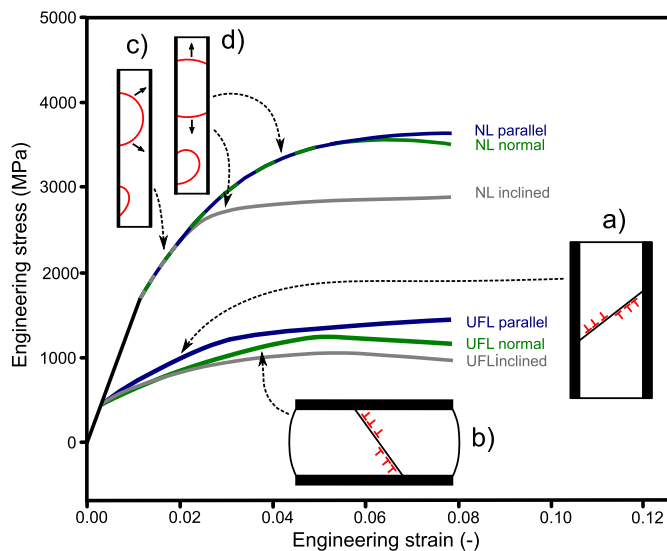


Fig. 7. Schematic of the assumed dominant plastic deformation processes within the ferrite in the major strain hardening regime, which is pile-up formation for the UFL a) parallel and b) normal orientation and c) dislocation generation from interfaces and consequent bulging through the lamellae for all NL pillars. d) Dislocation segments can move by bowing out parallel to the interface (confined layer slip) at larger stresses in the NL pillars.

For the discussion of this hardening one has to take into account that the NL pearlitic steel is a heavily deformed ferrite and cementite where the “cementite” is chemically and, therefore, mechanically not identical with the cementite of the UFL microstructure. This could explain the similar hardening rates and also the same strain values at the limit of strain hardening for the parallel and normal orientation in the NL structure, which is not observed for the UFL structure.

A lower strain hardening capacity was found for the inclined lamellae orientation, where plastic deformation or fracture of the cementite is not required for localization processes. Shear bands form parallel to the cementite lamellae and thereby terminate pronounced strain hardening in the end of deformation mode 2 (see video sequences in Supplementary). It is rather the case, that dislocation segments being stored within the ferritic channel at low strains, bow out and thereby, move within the ferrite lamellae when the Orowan stress σ_{or} is exceeded, according to

$$\sigma_{or} \sim 3\tau_{or} = \frac{Gb}{\pi(1-\nu)d} \ln\left(\frac{\lambda}{2\pi b}\right) \quad (8)$$

with the ferrite shear modulus G (80 GPa [37]), burgers vector b (0.248 nm), Poisson's ratio ν in the elastic case (0.29), lamellae thickness d and dislocation spacing $\lambda = \rho^{-1}$ with the dislocation density within the ferrite ρ ($8.8 \cdot 10^{15} \text{ m}^{-2}$ [29]). This rough approximation yields 3477 MPa and 2608 MPa for a 15 nm and 20 nm ferrite lamellae thickness, respectively, which is perfectly in the range of the hardening limit at 2650 MPa for the inclined loading condition. Thus, it seems that for the inclined loading situation not the yield or fracture stress of the cementite, but the bowing of dislocation segments in the confined situation of the narrow ferrite lamellae is the critical step for the formation of shear bands and subsequently shuts off the strain hardening. Such dislocation mechanisms, better known as confined layer slip (CLS), are frequently reported to operate in multilayers below a layer thickness of 50 nm [31]. It is very likely, that CLS also operates within the ferritic phase of the parallel and normal orientations at larger strains as schematically shown in Fig. 7d, but there it will certainly not trigger the onset of localized deformation.

One may assume that the crystal orientation in the UFL and the texture in the NL pillars should affect the flow stress and the hardening behavior. However, the yield stress and the hardening rate in the NL normal and parallel case are very similar. Also for the UFL the onset of yielding is in a similar range, as well as the hardening rate for the normal and inclined lamellae orientation. Therefore, we assume that the impact of the crystal orientation is

minor compared to the lamellar architecture.

4.3. The stress–strain behavior at larger strains

For both pearlitic structures a stress plateau forms, when the cementite starts to plastically deform or confined layer slip in the ferrite sets in. Within this region local stress drops $\Delta\sigma_{drop}$ appear for the NL normal, UFL normal and 22°-inclined micro pillars, when the shear bands have fully transversed the pillar width (see [Supplementary Fig. 2](#) and video sequences). These stress drops are quantified in [Table 2](#). Localized deformation terminates the pronounced hardening and only weak hardening or even softening occurs, mainly depending on the specific deformation mechanisms during strain localization of the lamellae orientation. Whereas localized deformation via kink bands sustains moderate hardening, localization in shear bands causes strain softening. Consequently, the strength at 5% plastic strain is for the parallel lamellae orientation somewhat larger as for the normal loaded lamellae irrespective of the lamellae thickness. Although the inclined oriented pillars deform both via shear bands, strain softening occurs for the UFL and strain hardening for the NL state. This could be the consequence of a very pronounced localization in one single shear band in the UFL state (geometrical softening), whereas in the NL state it is more homogeneously distributed in multiple shear bands.

4.4. The deformation behavior at larger strains

For the parallel oriented micro pillars pronounced kink band formation is observed in the UFL ([Figs. 3a and 4a](#)) and NL state ([Figs. 3d and 5a](#)), which seems to be the inherent deformation mechanism whenever the cementite lamellae are axially loaded under compression. Similar observation were made by Porter et al. [8] and Toribio et al. [18] in pearlitic wires, where cementite lamellae laterally loaded under compression deformed via kinking and buckling. At total strains above about 5% the collective kinking of lamellae leads to a localization of plastic deformation in terms of one pronounced kink band extended in a broader range of the pillar height (NL state, [Fig. 5a](#)) or in many little kink bands distributed along the pillar height (UFL state, [Fig. 4a](#)).

For the NL and UFL normally oriented micro pillars the deformation characteristics visible in SEM images of the side surface are almost identical ([Fig. 3b and e](#)). Both localize via shear band formation at total strains larger than 5%. Unlike earlier work from Porter et al. [8] a breaking of the harder cementite phase probably caused by interphase crossing of dislocations within the shear bands of the UFL pearlitic steel is not observed. The cross section images from the UFL pillar ([Fig. 4b](#)) confirm a bending and elongation of the cementite in the shear direction, which coincides with earlier observations of a ductile behavior of cementite [7]. Consistent layers within shear bands have also been reported for different types of nanoscaled multilayers, such as CuNb [38,39] or Cu-PdSi [40] and lead combined with the present SEM-investigations to the assumption, that also for the NL pearlitic steel the cementite stays intact. Although interface crossing by dislocations [28] cannot be excluded, the realignment of the ferrite lamellae in the shear direction visible in the cross section ([Fig. 5b](#)) accounts for a ductile

deformation and consistency of the cementite [35].

It could be demonstrated that not the interlamellar spacing but rather the lamellae orientation is determining the present deformation, localization and failure mechanism, which is in good agreement with earlier works from Porter et al. about tensile tests on coarse and fine lamellar pearlitic steels [8]. A similar strong lamella orientation influence has been also found for the fracture behavior [13,14]. The initial step for localization in the parallel and normal oriented pillars is the deformation of the harder cementite phase. This is not the case for the inclined lamellae orientation, since shear bands can easily propagate via confined layer slip of dislocations parallel to the harder cementite phase [8,41]. This is further confirmed by the absence of kinking or bending of the cementite suggesting Orowan bowing of dislocation loops within the ferritic lamellae.

4.5. Remarks to the macro behavior of a pearlitic steel

The UFL micro pillars are fabricated within one colony and therefore represent a composite array of single crystals. A polycrystalline pearlitic steel contains abundant colonies with various lamellae orientations. Hence, one could assume that the mechanical response of the macroscopic sample lies between the extreme cases of the parallel micro pillar with the highest strength and the 45°-inclined one with the lowest strength. From the stress–strain curve in [Fig. 2a](#) it becomes clear, that the macroscopic response approaches more to the 45°-inclined micro pillar at low strains and to the 22°-inclined one at larger strains. We conclude, that the macroscopic stress–strain behavior is dominated by the “softer” colonies with similar inclined orientations as present in the single colony specimens.

In addition to an intrinsic size effect due to the reduced lamellae spacing, also an extrinsic sample size effect has recently been reported for Cu/Zr multilayers [42] similar as observed earlier for copper single crystals [43]. However, the yield stress at 0.2% plastic strain of the macroscopically sized UFL compression samples ($3 \times 3 \times 6 \text{ mm}^3$) with 549 MPa is well within the range of the UFL micro pillars ($3 \times 3 \times 6 \text{ }\mu\text{m}^3$). Hence, for a UFL pearlitic steel down to a sample size of 3 μm an extrinsic sample size effect is not apparent. Since the number of layers per sample volume is even higher in the NL pillars, it is evident that the presented data of the micron-sized pillars represent a bulk-like behavior.

5. Conclusion

We have presented micro compression experiments of a nano-lamellar, NL, and ultrafine-lamellar, UFL, pearlitic steel, where special focus was put onto the influence of the ferrite and cementite lamellae orientation on the mechanical response. Micro pillars were FIB milled with the lamellae being aligned parallel, normal and inclined to the loading direction. The results indicate that both, the interlamellar spacing and the lamellae orientation, have a strong influence on the mechanical response and deformation characteristics. In particular it could be shown that:

- i) The yield stress measured at 0.2% plastic strain is largely affected by the interlamellar spacing. Hence, HPT deformation ($\epsilon_{\text{equ}} \sim 15$) causes a yield strength increase up to three times as a consequence of the stronger confinement of the dislocation within the ferrite lamellae. Surprisingly, the effect of lamellar orientation on $\sigma_{0.2}$ is not very pronounced.
- ii) Both, the NL and UFL pearlitic steel show a strong initial hardening followed by a stress plateau regime.

Table 2

Initial stress drops occurring in the UFL normal, UFL 22°-inclined and NL normal micro pillars, when a local shear band fully transverses the pillar width (see [Supplementary](#)).

	UFL normal	UFL 22°-inclined	NL normal
$\Delta\sigma_{drop}$ [MPa]	173	281	1124
ϵ_{drop} [%]	7.4	9.1	19.0

- iii) The interlamellar spacing and the orientation with respect to the loading direction has a significant effect on the hardening capacity.
- iv) The strong orientation effect on the initial hardening in the UFL microstructure can be explained by a composite model, where plastic deformation is governed by the ferrite, while the cementite deforms elastically.
- v) The hardening in the NL structure is even stronger, however, the onset of the plateau regime is sensitive to the lamellar orientation. The exceptional strain hardening capacity seems to be a consequence of the movement of single dislocation loops in such fine scaled structures instead of pile-up formation.
- vi) The deformation and failure mechanisms at large strains are controlled also by the orientation of the lamellae with respect to the loading direction. Whereas deformation of the cementite in the UFL and NL state is not incorporated in the shear band formation of the inclined orientation, ductile bending in the shear direction is required for the normal and kinking for the parallel orientation (UFL).

Acknowledgments

The authors would like to thank Prof. Daniel Kiener for valuable discussion. Financial support by the FWF Austrian Science Fund within project number P24429-N20 is gratefully acknowledged.

Appendix A. Supplementary data

Supplementary data related to this article can be found at <http://dx.doi.org/10.1016/j.actamat.2015.12.037>.

References

- [1] R.Z. Valiev, R.K. Islamgaliev, I.V. Alexandrov, Bulk nanostructured materials from severe plastic deformation, *Prog. Mater. Sci.* 45 (2000) 103–189.
- [2] M.A. Meyers, A. Mishra, D.J. Benson, Mechanical properties of nanocrystalline materials, *Prog. Mater. Sci.* 51 (2006) 427–556.
- [3] R.Z. Valiev, Y. Estrin, Z. Horita, T.G. Langdon, M.J. Zehetbauer, Y.T. Zhu, Producing bulk ultrafine-grained materials by severe plastic deformation, *JOM* 58 (2006) 33–39.
- [4] A. Zhilyaev, T.G. Langdon, Using high-pressure torsion for metal processing: fundamentals and applications, *Prog. Mater. Sci.* 53 (2008) 893–979.
- [5] F. Wetscher, A. Vorhauer, R. Stock, R. Pippan, Structural refinement of low alloyed steels during severe plastic deformation, *Mater. Sci. Eng. A* 387–389 (2004) 809–816.
- [6] J. Embury, R. Fisher, The structure and properties of drawn pearlite, *Acta Metall. Mater.* 14 (1966) 147–159.
- [7] G. Langford, Deformation of pearlite, *Metall. Trans. A* 8 (1977) 861–875.
- [8] D.A. Porter, K.E. Easterling, G.D.W. Smith, Dynamic studies of the tensile deformation and fracture of pearlite, *Acta Metall. Mater.* 26 (1978) 1405–1422.
- [9] D. Raabe, P. Choi, Y. Li, et al., Metallic composites processed via extreme deformation: toward the limits of strength in bulk materials, *MRS Bull.* 35 (2010) 982–991.
- [10] Y. Li, D. Raabe, M. Herbig, P. Choi, S. Goto, A. Kostka, H. Yarita, C. Borchers, R. Kirchheim, Segregation stabilizes nanocrystalline bulk steel with near theoretical strength, *Phys. Rev. Lett.* 113 (2014) 106104.
- [11] F. Wetscher, B.H. Tian, R. Stock, R. Pippan, High pressure torsion of rail steels, *Mater. Sci. Forum* 503–504 (2006) 455–460.
- [12] F. Wetscher, R. Pippan, S. Sturm, F. Kauffmann, C. Scheu, G. Dehm, TEM investigations of the structural evolution in a pearlitic steel deformed by high-pressure torsion, *Metall. Mater. Trans. A* 37 (2006) 1963–1968.
- [13] A. Hohenwarter, A. Taylor, R. Stock, R. Pippan, Effect of large shear deformations on the fracture behavior of a fully pearlitic steel, *Metall. Mater. Trans. A* 42 (2011) 1609–1618.
- [14] C. Kammerhofer, A. Hohenwarter, S. Scheriau, H.P. Brantner, R. Pippan, Influence of morphology and structural size on the fracture behavior of a nanostructured pearlitic steel, *Mater. Sci. Eng. A* 585 (2013) 190–196.
- [15] Y. Ivanisenko, W. Lojkowski, R.Z. Valiev, H. Fecht, The mechanism of formation of nanostructure and dissolution of cementite in a pearlitic steel during high pressure torsion, *Acta Mater.* 51 (2003) 5555–5570.
- [16] X. Sauvage, Y. Ivanisenko, The role of carbon segregation on nanocrystallisation of pearlitic steels processed by severe plastic deformation, *J. Mater. Sci.* 42 (2007) 1615–1621.
- [17] Y.J. Li, P. Choi, C. Borchers, S. Westerkamp, S. Goto, D. Raabe, R. Kirchheim, Atomic-scale mechanisms of deformation-induced cementite decomposition in pearlite, *Acta Mater.* 59 (2011) 3965–3977.
- [18] J. Toribio, E. Ovejero, Effect of cumulative cold drawing on the pearlite interlamellar spacing in eutectoid steel, *Scr. Mater.* 39 (1998) 323–328.
- [19] J. Toribio, Relationship between microstructure and strength in eutectoid steels, *Mater. Sci. Eng. A* 387–389 (2004) 227–230.
- [20] M.D. Uchic, D.M. Dimiduk, J.N. Florando, W.D. Nix, Sample dimensions influence strength and crystal plasticity, *Science* 305 (2004) 986–989.
- [21] A. Hohenwarter, A. Bachmaier, B. Gludovatz, S. Scheriau, R. Pippan, Technical parameters affecting grain refinement by high pressure torsion, *Int. J. Mater. Res.* 100 (2009) 1653–1661.
- [22] S. Wurster, C. Motz, M. Jenko, R. Pippan, Micrometer-sized specimen preparation based on ion slicing technique, *Adv. Eng. Mater.* 12 (2010) 61–64.
- [23] S. Wurster, R. Tremel, R. Fritz, M.W. Kapp, et al., Novel methods for the site specific preparation of micromechanical structures, *Prakt. Metallogr. Pr. M.* 52 (2015) 131–146.
- [24] D. Kiener, C. Motz, M. Rester, M. Jenko, G. Dehm, FIB damage of Cu and possible consequences for miniaturized mechanical tests, *Mater. Sci. Eng. A* 459 (2007) 262–272.
- [25] H. Zhang, B.E. Schuster, Q. Wei, K.T. Ramesh, The design of accurate micro-compression experiments, *Scr. Mater.* 54 (2006) 181–186.
- [26] H. Wörgötter, D. Kiener, J.M. Purswani, D. Gall, G. Dehm, Testing thin films by microcompression: benefits and limits, *BHM* 153 (2008) 257–262.
- [27] S. Wurster, C. Motz, R. Pippan, Characterization of the fracture toughness of micro-sized tungsten single crystal notched specimens, *Philos. Mag.* 92 (2012) 1803–1825.
- [28] A. Misra, J.P. Hirth, R.G. Hoagland, Length-scale-dependent deformation mechanisms in incoherent metallic multilayered composites, *Acta Mater.* 53 (2005) 4817–4824.
- [29] X. Zhang, A. Godfrey, X. Huang, N. Hansen, Q. Liu, Microstructure and strengthening mechanisms in cold-drawn pearlitic steel wire, *Acta Mater.* 59 (2011) 3422–3430.
- [30] M. Srinivas, G. Malakondaiah, R.W. Armstrong, P. Rama Rao, Ductile fracture toughness of polycrystalline armco iron of varying grain size, *Acta Metall. Mater.* 39 (1991) 807–816.
- [31] A. Misra, M. Verdier, Y.C. Lu, H. Kung, T.E. Mitchell, M. Nastasi, J.D. Embury, Structure and mechanical properties of Cu-X (X=Nb,Cr,Ni) nanolayered composites, *Scr. Mater.* 39 (1998) 555–560.
- [32] J. Gil Sevillano, P. van Houtte, E. Aernoudt, Large strain work hardening and textures, *Prog. Mater. Sci.* 25 (1980) 69–134.
- [33] L. Thilly, M. Véron, O. Ludwig, F. Lecouturier, J.P. Peyrade, S. Askénazy, High-strength materials: in-situ investigations of dislocation behaviour in Cu-Nb multifilamentary nanostructured composites, *Philos. Mag. A* 82 (2002) 925–942.
- [34] B. Karlsson, G. Lindén, Plastic deformation of eutectoid steel with different cementite morphologies, *Mater. Sci. Eng.* 17 (1975) 153–164.
- [35] J.D. Embury, J.P. Hirth, On dislocation storage and the mechanical response of fine scale microstructures, *Acta Metall. Mater.* 42 (1994) 2051–2056.
- [36] M. Janecek, F. Louchet, B. Doisneau-Cottignies, Y. Bréchet, N. Guelton, Specific dislocation multiplication mechanisms and mechanical properties in nano-scaled multilayers: the example of pearlite, *Philos. Mag. A* 80 (2009) 1605–1619.
- [37] G.R. Speich, A.J. Schwobbe, W.C. Leslie, Elastic constants of binary iron-base alloys, *Metall. Trans.* 3 (1972) 2031–2037.
- [38] N.A. Mara, D. Bhattacharyya, J.P. Hirth, P. Dickerson, A. Misra, Mechanism for shear banding in nanolayered composites, *Appl. Phys. Lett.* 97 (2010) 021909.
- [39] S.J. Zheng, J. Wang, J.S. Carpenter, W.M. Mook, P.O. Dickerson, N.A. Mara, I.J. Beyerlein, Plastic instability mechanisms in bimetallic nanolayered composites, *Acta Mater.* 79 (2014) 282–291.
- [40] I. Knorr, N.M. Cordero, E.T. Lilleodden, C.A. Volkert, *Acta Mater.* 61 (2013) 4984–4995.
- [41] A. Misra, J.P. Hirth, R.G. Hoagland, J.D. Embury, H. Kung, Dislocation mechanisms and symmetric slip in rolled nano-scale metallic multilayers, *Acta Mater.* 52 (2004) 2387–2394.
- [42] J.Y. Zhang, S. Lei, Y. Liu, J.J. Niu, Y. Chen, G. Liu, X. Zhang, J. Sun, Length scale-dependent deformation behavior of nanolayered Cu/Zr micropillars, *Acta Mater.* 60 (2012) 1610–1622.
- [43] D. Kiener, W. Grosinger, G. Dehm, R. Pippan, A further step towards an understanding of size-dependent crystal plasticity: in situ tension experiments of miniaturized single-crystal copper samples, *Acta Mater.* 56 (2008) 580–592.